Chapter 10

Tree Structure for Modeling Skin Lesion Growth

Tim K. Lee,[*,†,‡,§] *Sina Khakabi,*[‡] *Paul Wighton,*[#] *Harvey Lui,*[*,†] *David I. McLean*[†] *and M. Stella Atkins*[†,‡]

[*] *Departments of Cancer Control Research and Integrative Oncology, BC Cancer Agency, Vancouver, Canada*
[†] *Photomedicine Institute, Department of Dermatology and Skin Science, University of British Columbia and Vancouver Coastal Health Research Institute, Vancouver, Canada*
[‡] *School of Computing Science, Simon Fraser University, Burnaby, Canada*
[#] *Martinos Center for Biomedical Imaging, Harvard Medical School, Boston, USA*
[§] *Email: tlee@bccrc.ca*

Cutaneous malignant melanoma is one of the most frequent types of cancer in the world; but if the malignancy is detected and treated early, it can be cured. Many dermatologists promote dermoscopy as an early detection tool; however, dermoscopy requires formal training with a steep learning curve. In this chapter, we introduce a novel tree-based framework to automate the melanoma detection from dermoscopic images. Inspired by the radial and vertical growth pattern of skin lesions, we designed a flexible and powerful framework by decomposing dermoscopic images recursively. Pixels are repeatedly clustered into sub-images according to the color information and spatial constraints. This framework allows us to extract features by examining the tree from a graphical aspect, or from a textural/geometrical aspect on the nodes. In order to demonstrate the effectiveness of the proposed framework, we applied the technique, in completely different manners, to two common tasks of a computer-aided diagnostic system: segmentation and classification. The former task achieved a per-pixel sensitivity and specificity of 0.89 and 0.90 respectively on a challenging data set of 116 pigmented skin lesions. The latter task was tested on a public data set of 112 malignant and 298 benign lesions. We obtained 0.86 and 0.85 for precision and recall, respectively, along with an F-measure of 0.83 using a 3-layer perceptron. These experiments testified the versatility and the power of the tree-structure framework for dermoscopic analyses.

1. Introduction

Malignant melanoma of the skin, a life-threatening disease, has been increasing rapidly and steadily among fair-skinned populations over last few decades. In British Columbia, Canada, a low sun country of the world, the incidence rate has been tripled since 1970's.[1] South of Canada, the USA recorded a 3.1% average annual increase.[2] In Australia, melanoma has surpassed lung cancer as the third most common cancer for both men and women and the most common cancer for men between the age of 15 and 44.[3] Overall, the disease has become a major health problem for the countries with a large white population.

Malignant melanoma is very treatable if it is detected early. The five-year survival rate is greater than 90%. However, the prognosis is poor for many patients with advanced or late staged disease. For these patients, the 5-year survival rate can reduce dramatically to only 15% after their initial diagnosis.[4] Thus, early detection is essential for a successful treatment of the disease.

Early melanoma detection is, however, challenging because the malignancy often resembles benign lesions such as melanocytic nevi and seborrheic keratoses.[5,6] Diagnosis with naked eyes often results in false negatives or false positives.[5,7,8] In order to improve the diagnostic accuracy, many experts have been advocating the use of a non-invasive hand-held device, dermoscopy, which provides a magnified view of the skin internal structure.[9] Applying either polarized light or oil immersion to render the outermost layer of the skin, epidermis to be translucent, physicians who have specially trained for the technique can examine the morphology of the skin lesion at the dermal-epidermal junction and render a diagnosis. (Figure 1 shows two examples of dermoscopic images.) Studies showed that this non-invasive technique improved the diagnostic accuracy only for the trained physicians. Untrained doctors, even dermatologists, are often confused by the complex and unfamiliar visual patterns, thereby reducing their diagnostic capability.[9] Recently, many research groups have been developing automated computer algorithms to assist physicians in analyzing the complex dermoscopic patterns in the hope to neutralize the steep learning curve of the technique. The common approach is to detect and analyze various dermoscopic structures such as pigment networks, streaks and blood vessels.[10–14] This approach achieves various degrees of success.

In this chapter, we introduce a new framework for automatic analysis of dermoscopic images. It is a novel approach inspired by the analysis of the growth pattern of skin lesions. In this approach, a dermoscopic image is decomposed using a simple growth model estimated using a single image; then a tree-structure is constructed to represent the growth model.

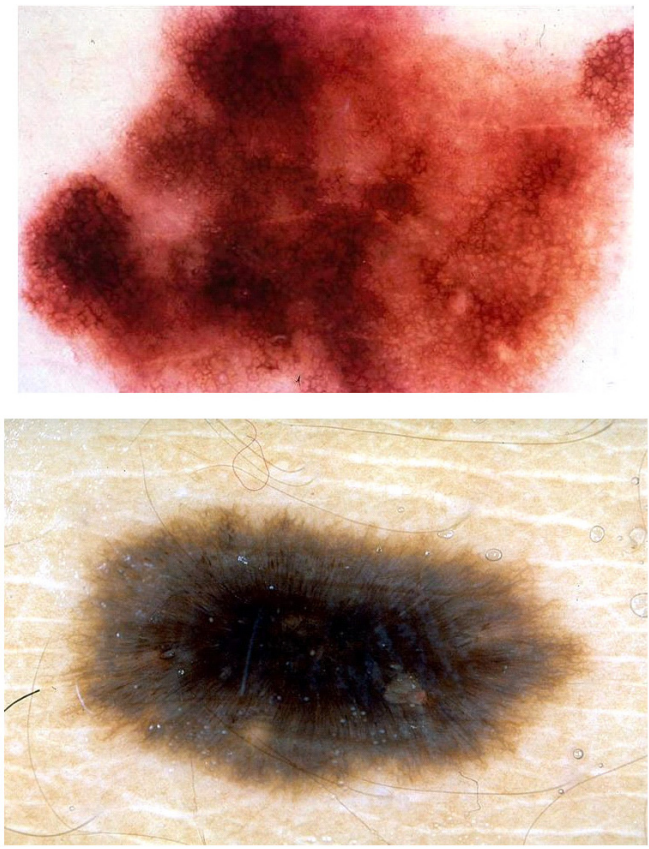

Fig. 1. Samples of dermoscopic images. The top lesion has an irregular shape, while the bottom figure has a regular oval shape.

The remaining of the paper is organized as follows: the next section reviews the lesion growing model and previous works on decomposition. Section 3 describes the construction of the tree-based framework, a very flexible structure allowing it to adopt for various scenarios and needs. Sections 4 and 5 demonstrate the flexibility of the technique by applying it to two common tasks of a computer-aided diagnostic system: lesion segmentation and classification. Finally, a short conclusion is presented in Section 6.

2. Background and Previous Work

2.1. *Lesion Growth Model*

Cuteneous malignant melanomas are often identified with two growth phases: radial and vertical.[15] Both malignant and benign pigmented skin lesions usually

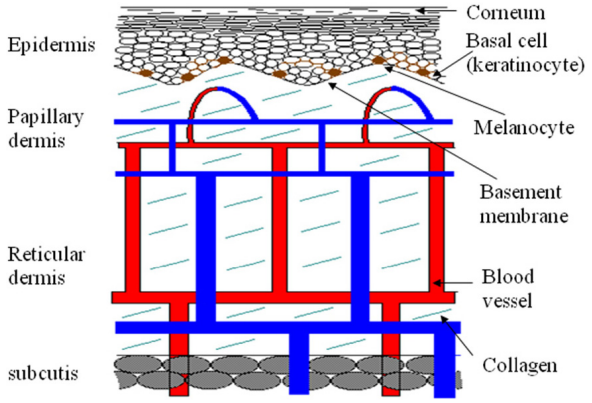

Fig. 2. Schematic of the epidermis and dermis strcutures.

begin with a radial growth. In this phase, a pigmented lesion is formed by nests of melanocytes, which synthesize a brown pigmentation called melanin. This phase commences at the dermal-epidermal junction and the entire horizontal growth phase is confined in epidermis, the outer layer of the skin. The vertical growth phase is marked by the penetration of the basement membrane of the outer skin into the dermis. (Figure 2 depicts the structure of the epidermis and dermis.) During the growth of a lesion, the width and depth of the lesion extend out from the initial melanocytic nest of the lesion. Due to the natural history of normal and abnormal cells, benign skin lesions tend to grow evenly, often in a regular oval shape, while abnormal lesions often result in an irregular shape. (Figure 1 illustrates two lesions, one with an irregular shape and another one with a regular oval shape.)

Using a single dermoscopic image, the growth pattern of a pigmented lesion can be postulated because the center the lesion is often the initial melanocytic nest. Zhou *et al.* utilized this hypothesis[16] and observed that most dermatologists placed the center of the lesion in the middle of a dermoscopic image frame, and constrained a segmentation algorithm spatially by assuming the middle of the image frame as the initial growing point of the lesion. We further observed that the periphery of a skin lesion often has a lighter brown color than the interior of the lesion. This phenomenon could be explained by the fact that the center of the lesion is usually thicker with more layers of melanocytes than the newly grown areas near the periphery. Because melanin absorbs light, the central area tends to have less reflected light and, hence, darker than the periphery. Thus, we modified Zhou *et al.*'s growth model in the following way: the center of a skin lesion is determined by the dark-color

portion of the skin lesion. Based on this extended growth model, we decompose the skin image into a tree structure.

2.2. *Decomposition*

Shape and image decomposition can be categorized into boundary-based or area-based approaches. The former method has been successfully used to analyze border irregularity of a lesion by decomposing a lesion border into a series of indentation and protrusion segments.[17] However, in order to analyze the growth pattern of a lesion, an area-based method is required to analyze the image texture. There are many successful ways to perform area-based decomposition, such as morphological shape decomposition and skeleton decomposition.[18] Unfortunately, a pigmented skin lesion may manifest one or more of the following patterns: reticular, globular, cobblestone, starburst, parallel and homogeneous. In addition, the spatial relationship between any texture patterns is unknown. Hence, it is a nontrivial task to design an optimal structural element for the morphological operations. On the other hand, skeleton decomposition is the complement problem of boundary decomposition; both depend strongly on the border shape and may not reflect the internal texture patterns. In this chapter, a new decomposition method by clustering is proposed. The method represents the growth pattern of the lesion.

3. Decomposing Skin Images into Tree Structures

Unlike Zhou *et al.*'s approach,[16] our goal is to represent the growth pattern of a skin lesion by creating a tree structure. this chapter assumes that the center of the lesion (or part of a lesion in the middle of the recursion) is defined by the center of the dark pixels of the lesion. The central point is used to constraint the clustering the image pixels into dark and light regions. The identification of the central point and clustering are performed recursively in order to decompose a skin region into two sub-regions, which are also marked as the node of a tree. Thus the tree-building process can be divided into three subtasks: identifying the central point, clustering the image pixels and constructing the tree.

3.1. *Extraction of the Central Point*

Let us denote a pixel p of a color skin lesion image by its image coordinate (x, y). A set of connected pixels CP can be divided into dark and light pixels according to their luminance intensities $I(x, y)$, normalized by the maximum

luminance intensity I_m. Thus, the coordinates of the dark pixels, denoted by the set $\{(DX, D\Upsilon)\}$, is defined as:

$$\{(DX, D\Upsilon)\} = \left\{(x, y) \left| \frac{I(x, y)}{I_m} \leq I_d \right.\right\}, \tag{1}$$

for all $p \in CP$. I_d is the pre-defined cut-off threshold for the dark pixels.

The central point (x_c, y_c) of CP is defined by the centroid of the dark pixels only. For n connected dark pixels as determined by Eq. (1), the centroid of CP is defined as:

$$(x_c, y_c) = \left(1/n \sum_{i=1}^{n} x_i,\ 1/n \sum_{i=1}^{n} y_i\right), \quad x_i \in DX, \quad y_i \in D\Upsilon. \tag{2}$$

Note that the detection of dark pixels in Eq. (1) is only for the determination of the central point. We hypothesize that a lesion expands from the central point (x_c, y_c), the centroid of the dark pixels, as it grows. Thus, an ideal normal skin lesion will have concentric circles or ellipses for the dark and light pixels as shown in Fig. 3. However, real lesions often show a complex shape, especially, for melanomas which consist of unstable malignant cells and produces irregular growth rate in different directions. Sometimes, the dark or light pixels may not form a connected component. Nevertheless, the scheme in the following section decomposes a skin lesion into a tree structure according to the distance from the central point (x_c, y_c), along with the color information of the lesion.

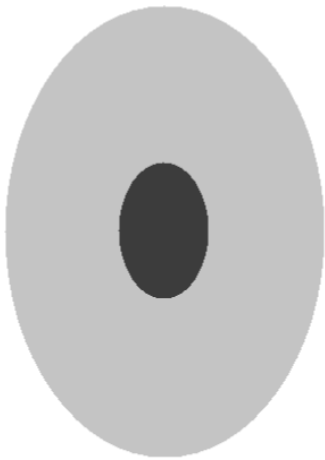

Fig. 3. The growth pattern of an ideal skin lesion, as shown in dark and light pixels. For this paper, the center point of the lesion is defined by the centroid of the dark pixels only.

3.2. *Clustering Decomposition*

A set of connected pixels *CP* is decomposed into two regions using the well-known k-means clustering algorithm, which minimizes the sum of squares of the distance between the feature (variable) associated with the pixels of the region and the region centroids.[19,20] For the dark and light regions, i.e. $k = 2$, the k-means clustering is formulated as:

$$\arg\min_{S} \sum_{i=1}^{2} \sum_{f_j \in S_i} \frac{1}{w_i} \|f_j - \mu_i\|^2, \tag{3}$$

where f_j is the j feature (variable) of the region, and μ_i is the centroid of the region S_i. For our task, one spatial feature and two chromatic features are applied in the clustering algorithm: the radial distance D and the blue and green intensity channels of the RGB color image. The red channel is eliminated in order to reduce the effect of the blood vessels. The radial distance D of a pixel (x, y) is defined as the Euclidean distance between the pixel and the central point of the original connected pixels *CP*, which is computed by Eq. (2). The features are weighted by w_i. Such a weight is especially important for the radial distance D because too strong a weight on D places the emphasis on the spatial feature over the chromatic features and results artificially rounded regions. After clustering, the parent region formed by *CP* is divided into two disjoint sibling regions CP_1 and CP_2.

3.3. *Tree Construction*

The root node of the tree structure is initialized to the cluster of all pixels of the skin lesion image. Then the nodes for the subsequent depth is built recursively by clustering the pixels of the parent's node into the two disjoint sibling regions (CP_1 and CP_2), using 2-means clustering, according to the distances to the centroid of the parent nodes and the red and blue intensity values. The termination condition varies according to the analysis need. As demonstrated in the following sections, a tree with a fixed depth is used in the segmentation task, while a tree with variable length is constructed for lesion diagnosis.

The resultant tree structure has two important properties:

(1) Summation of the pixel counts at every level of the tree is equal to the number of pixels in the original image, and
(2) Every pixel belongs to exactly one cluster at every level of the tree.

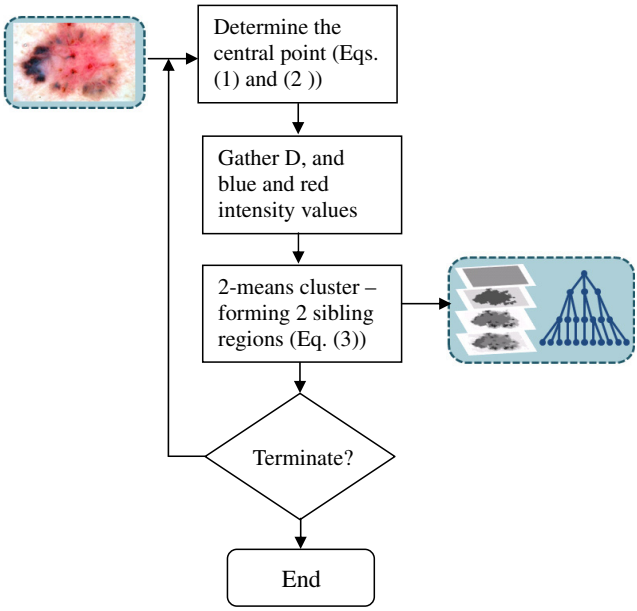

Fig. 4. Flowchart of the image decomposition process.

These two properties along with the flexibility of the termination condition during the tree construction provide a rich representation over which many salient features of the color skin lesion can be extracted.

The flowchart of the decomposition process and tree construction is shown in Fig. 4, outlining the entire process from an input image to the final tree structure.

4. Skin Lesion Segmentation

The usefulness of the tree representation is first demonstrated in a skin lesion segmentation application. The tree is constructed with the following parameters. The cut-off intensity I_d in Eq. (1) was set to 0.25, and the weights w_j in Eq. (2) were set to 2 for the radial distance D, and to 1 for both blue and green channels. In addition, the depth of the tree was set to 4. In other words, after decomposing a color skin image, the root level places all image pixels into one cluster, and other level decomposes the pixels into different clusters according to the procedure described in Section 3. Because a RGB color image consists of 3 intensity channels, the tree decomposition method generates 12 intensity images (3 color channels and 4 depth levels) as shown

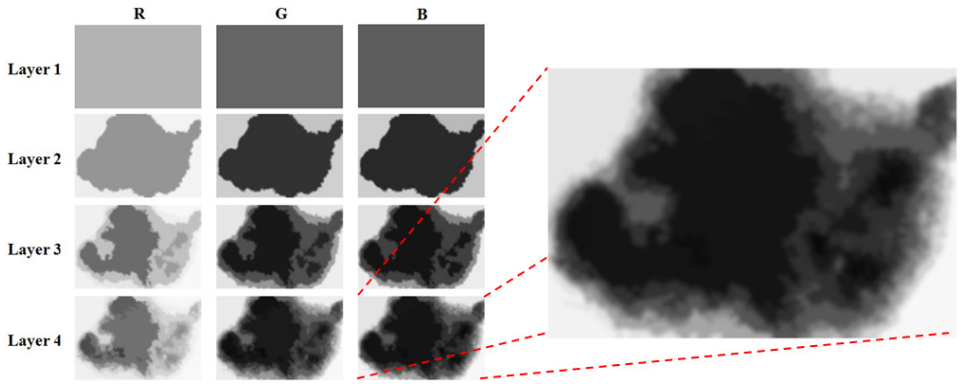

Fig. 5. Decompose the top figure of Fig. 1 for segmentation. The tree has 4 levels and 3 channels in each level.

in Fig. 5. The intensity value in each cluster is first assigned to the mean cluster intensity value. Then each intensity image was smoothed by a 15×15 Gaussian filters with $\sigma = 5$.

A feature vector of 13 elements was extracted for each pixel using the above data representation. The feature elements were the 12 intensity values in all levels and color channels, along with a spatial feature, the Euclidean distance between the pixel and the center of the lesion (x_c, y_c) of the root level. The feature vector was applied to a MAP estimation based on supervised learning model for automated skin lesion analysis.[21] The label set for the segmentation task in this model was $L = \{$'*lesion*'; '*background*'$\}$.

The first stage in the supervised learning model was the training stage in which parameters for the multivariate Gaussian distribution were estimated for the labeling phase. The posterior probabilities $P(p_j|l_i)$ (i.e. probability of a pixel p given the label l_i in the label set L) were modeled as multivariate Gaussian distribution. In the second stage which was the labeling stage, labels l^* were assigned to the pixels of previously unseen images using maximum likelihood estimation in the following way:

$$l^* = \arg\max_{l_i \in L} (\log P(p|l_i) + \log P(l_i)). \tag{4}$$

As in this case there were two classes $l_1 = lesion$ and $l_2 = background$, the following constraint was considered:

$$P(l_1) + P(l_2) = 1. \tag{5}$$

The ROC curve was obtained by varying the values of $P(l_1)$ and $P(l_2)$ according to constraint in equation above. Equivalently, the ROC curve could

be generated using a simple threshold method over the pixel probability map obtained using the following equation:

$$l_i(p) = \frac{P(p|l_i)}{P(p|l_2) + P(p|l_2)}, \tag{6}$$

where $l_i(p)$ is the likelihood of each label.[21]

The segmentation method was tested in a dataset, which has been used in several segmentation algorithms. The dataset contained 116 images of which 100 were considered challenging from a dermoscopic atlas.[22] An image is considered challenging if at least one of the following conditions are true[21]:

(1) the contrast between skin and lesion is low,
(2) there is significant occlusion by oil or hair,
(3) the entire lesion is not visible (partial lesion),
(4) the lesion contains variegated colors, or
(5) the lesion border is not clearly defined.

In addition, each image was segmented by a dermatologist to provide the ground truth, and pixels were labeled from the set L = {'*lesion*'; '*background*'}. Ten-fold cross-validation was used to validate the method.

Examples of five segmentation results from our method are provided in Fig. 6, where the first row is an easy image to segment and the remaining rows are the challenging cases containing lesions occluded with hair, partial lesions and low contrast borders of the lesions. No pre-processing of removing hairs or noise is applied to this segmentation test of the data representation.

The segmentation results are tabulated in Table 1 along with six other state-of-the-art skin lesion segmentation techniques: G-LoG/LDA,[21] KPP,[16] JSEG,[23] DTEA,[24] SRM,[25] and FSN.[26] The dataset was tested using the authors' implementation of their methods. Similar to G-LoG/LDA,[21] the output of the current method is a probability map of the pixels. Consequently, by changing the threshold of the segmentation over this probability map, the ROC curves were obtained (see Fig. 7). The output of the five other methods is binary segmentation of lesions; therefore, the nearest point on the ROC curve was compared with the sensitivity/specificity pairs. Table 1 lists ΔSens and ΔSpec, which show the difference between the sensitivity/specificity of methods with the closest pair on ROC curve of the current method. The area under the curve is only used to compare the current method with G-LoG/LDA in the column AUC. The sensitivity/specicity reported in the table for the current method and for G-LoG/LDA is the closest point to (0; 1), the optimal performance, on the ROC curve.

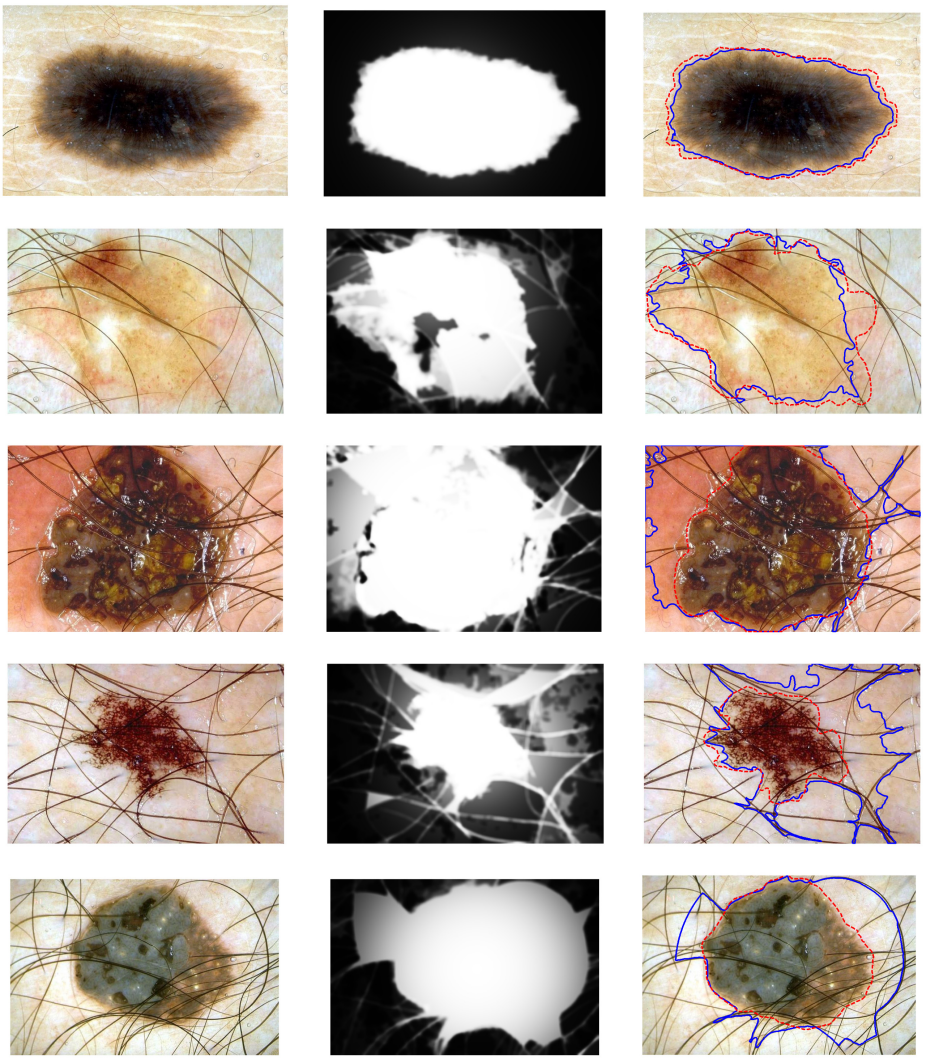

Fig. 6. Examples for the segmentation model. Examples of easy (first row) and challenging (second to the fifth rows) images are shown. The first column shows the original dermoscopic images. The second column demonstrates resulting probability maps obtained using the learning model. Our segmentation results and the ground-truth are depicted as blue and red dashed line, respectively, in the third column. Note: hair or noise removal pre-processing was not applied in this experiment.

The current method with tree decomposition achieved excellent AUC, sensitivity and specificity of 0.96, 0.89 and 0.90, respectively. These indicators showed that the technique outperformed G-LoG/LDA. The tree-based approach also outperformed KPP, DTEA, SRM, and FSN, and was comparable to JSEG's performance according to ΔSens and ΔSpec.

Table 1. Comparison of results of our segmentation method with six other methods.

Method	AUC	Sens.	Spec.	ΔAUC	ΔSens.	ΔSpec.
Our method	0.954	0.881	0.903	N/A	N/A	N/A
G-LoG/LDA	0.948	0.880	0.887	0.006	0.001	0.016
KPP	N/A	0.717	0.790	N/A	0.164	0.025
DTEA	N/A	0.641	0.987	N/A	0.035	−0.001
SRM	N/A	0.770	0.946	N/A	0.002	0.024
JSEG	N/A	0.678	0.986	N/A	−0.002	−0.001
FSN	N/A	0.812	0.935	N/A	0.012	0.017

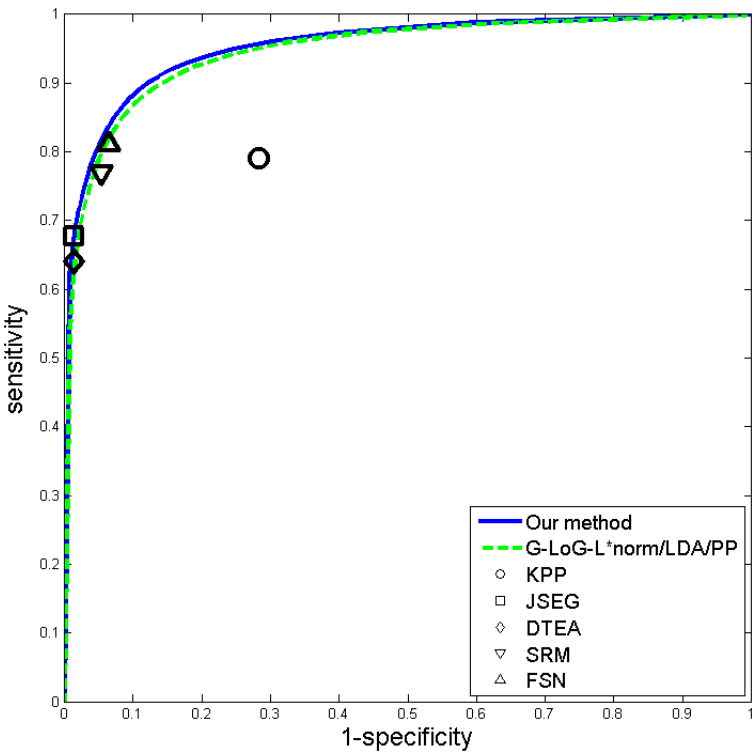

Fig. 7. Comparing the ROC curves for our method and six other methods, G-LoG/LDA,[21] KPP,[16] JSEG,[23] DTEA,[24] SRM,[25] and FSN.[26]

5. Skin Lesion Diagnosis

In the second experiment, we demonstrated the flexibility of the framework by modifying the decomposition process for a lesion diagnosis problem. The cut-off intensity I_d in Eq. (1) and the weights w_j for spatial parameter D and

chromatic channels in Eq. (2) were kept to 0.25, 1, and 2, respectively, similar to the skin lesion segmentation experiment. However, instead of using the RGB color channels, hue, saturation, and intensity of HSI color space were used in the k-means clustering procedure described in Section 3.2. There were two other major modifications for building the data structure: a tree structure with a variable depth is constructed and a cluster and shrink procedure is deployed for pruning one of the regions. During the tree construction, the lighter regions obtained from the k-means were pruned. Only the darker regions were kept and decomposed again. In additional, the following four conditions were set for the termination of the tree construction:

(1) A dark region was too small in size;
(2) A dark region consisted of similar colors;
(3) The decomposed dark region had not significantly changed in comparison to its parent; and
(4) The depth of the constructed tree reached a predefined limit.

When one of the above conditions was met, the decomposition terminated. Figure 8 depicts the resultant tree structure for a benign and an abnormal lesion.

Features used for analysing lesion condition were also changed. Observing the new tree structures in Fig. 8 for a typical benign and a malignant lesion, we realized that the tree itself (graphical aspect) could be used to differentiate the disease condition. Thus the following feature vector was selected: the number of nodes and leaves of the tree, the depth of the tree and the average compactness index for each level of the tree. Compactness index CI was defined as

$$CI = \frac{PE}{4\pi A}, \tag{7}$$

where PE and A denoted the perimeter and the corresponding area, respectively, of the darker region. The CI was calculated for all the nodes in the tree; then, the mean value of the all CIs over each depth of the tree was calculated and stored in the feature vector. Because the root region was rectangular, the CI for this node was ignored. Thus, the number of CIs was one less than the maximum possible depth of the tree which was defined in the termination condition.

The tree representation and the feature vector were tested in a two-class classification (malignant vs. benign) experiment, using a data set of 410 pigmented skin images randomly selected from Interactive Atlas of Dermoscopy.[27] In this dataset, there were 112 malignant lesion images (containing melanoma and pigmented basal cell carcinomas), and 298 benign lesion images (consisting

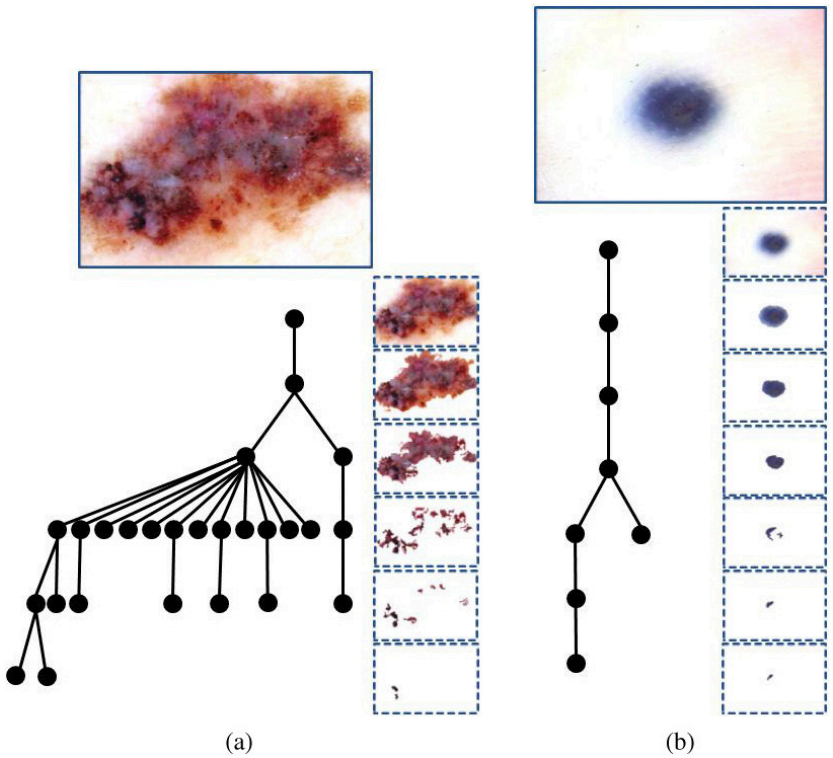

Fig. 8. The variable tree structures with the lighter region pruned for (a) a melanoma and (b) a benign lesion.

Table 2. Classification results for the two-class classification, benign and malignant, using a data set of 410 lesion images.

Feature set	Classifier	Precision	Recall	F-Measure	AUC of ROC
All features	3-layer perceptron	0.855	0.849	0.834	0.786
Graphical features	3-layer perceptron	0.848	0.841	0.824	0.787
CI1 to CI3	3-layer perceptron	0.639	0.712	0.641	0.617
CI4 to CI9	3-layer perceptron	0.713	0.729	0.622	0.494
All features	AdaBoost	0.829	0.832	0.817	0.745
Graphical Features	AdaBoost	0.835	0.837	0.823	0.776
CI1 to CI3	AdaBoost	0.692	0.732	0.685	0.637
CI4 to CI9	AdaBoost	0.596	0.722	0.614	0.490

of atypical, congenital, compound, dermal, Spitz, and blue nevi; seborrheic keratosis; and dermatofibroma). The ground truth was provided by the atlas.

Publicly available machine learning tools, a 3-layer perceptron and AdaBoost of WEKA[28] were used to classify the 410 images into malignant and benign. The parameters for the perceptron were set as follows: learning rate was set to 0.3, momentum was set to 0.2, training time was set to 500 and validation threshold was set to 20. The parameters of AdaBoost were set as follows: the number of iterations was set to 10, the seed was randomly generated and the weight threshold was set to 100.

The data set was tested in four different ways. In the first approach, all twelve features were gathered in a 12-dimensional feature set [number of nodes, number of leaves, depth, and 9 compactness index (*CI*) components] and the resulting set was fed into the two classifiers separately. The second evaluation was done by just using the graphical feature set (number of nodes, number of leaves, depth). In the third and fourth approaches, *CI1* to *CI3* and *CI4* to *CI9* were evaluated respectively to validate the discriminative power of different layers in the tree in our method. In all these approaches, the validation method was set to a ten-fold cross validation. The malignant and benign images were randomly chosen from separate classes and uniformly merged and distributed over the folds. Table 2 provides the classification results between the malignant and benign classes for our dataset using two classifiers and four approaches. Figure 9 shows the ROC curves from the 3-layer perceptron and AdaBoost classifiers.

Table 2 shows that using all features, both classifiers returned very good results in precision, recall and F-Measure. The 3-layer perceptron achieved 0.86, 0.85 and 0.83 for precision, recall and F-measure, respectively. The results for AdaBoost were slightly lower, but were above 0.8 for precision and recall. Interestingly, the graphical features alone were performing so well. They achieved similar performance as all features under the perceptron classifier, and they surpassed the all features results under the AdaBoost classifier. This illustrated the strength of the tree structure over the other methods that were only based on textural/geometrical features. These results also explained that the *CI1* to *CI3* feature set, the top three layers, had more discriminative power than the *CI4* to *CI9* feature set, the lower layer set.

The ROC curves in this study are obtained using WEKA machine learning software.[28] The reason behind the more jagged ROC curve for AdaBoost was likely due to the low density of the grid search over the parameters of the classifier. The denser grid for the 3-layer perceptron classifier results in the smoother curves.

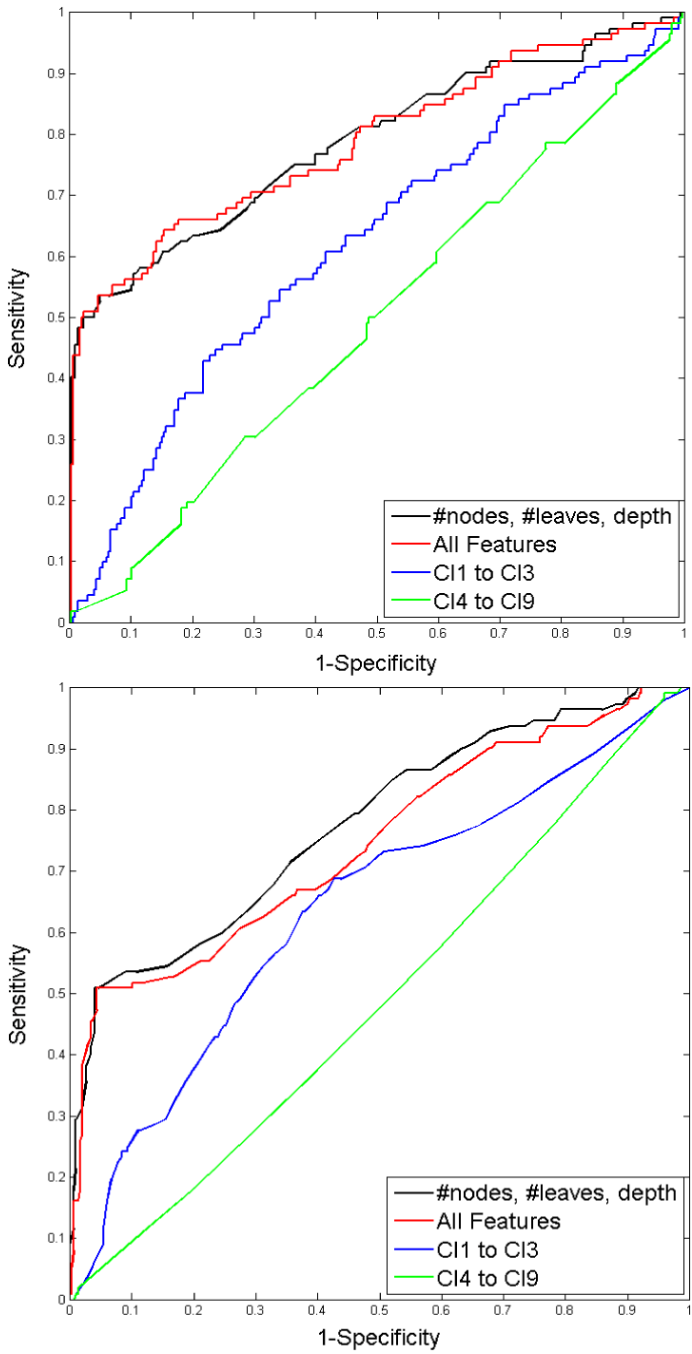

Fig. 9. ROC curves for (top) 3-layer perceptron and (bottom) AdaBoost classifiers for lesion diagnosis.

6. Conclusions

In this chapter, we introduce a novel tree structure-based framework for dermoscopic image analysis. Inspired by skin lesion growth patterns, we designed a flexible and powerful framework, which decomposes a skin image into a mutli-level tree structure. All pixels are represented uniquely in each level; hence, task-specific salient features can be extracted. In order to demonstrate the flexibility and the power of the framework, it was tested in two common skin image analysis tasks of segmentation and diagnosis. Both segmentation and diagnosis programs returns good and promising results. However, the configurations and the parameters for these two programs are not the emphasis of this chapter because we believe one can extract new features to future improve the results. The main focus is the tree structure framework itself, which can be applied to other skin image analysis tasks.

Acknowledgments

This work was supported in part by the Natural Sciences and Engineering Research Council of Canada (NSERC) and the Canadian Institute of Health Research (CIHR), and by a scholarship from the CIHR Skin Research Training Centre.

References

1. D. I. McLean, N. Phillips, Y. Zhou, R. Gallagher and T. K. Lee, "40-Year Trends in Skin Cancer in British Columbia, Canada, 1973 to 2003," *J Cutaneous Med Surg* **16**, 83–91 (2012).
2. E. Linos, S. M. Swetter, M. G. Cockburn, G. A. Colditz and C. A. Clarke, "Increasing burden of melanoma in the United States," *J Invest Dermatol* **129**, 1666–1674 (2009).
3. Australian Institute of Health and Welfare, "Cancer incidence projections Australia 2002 to 2011," Cat. no. CAN 25, Canberra, 166 (2005).
4. C. M. Balch, J. E. Gershenwald, S. J. Soong, J. F. Thompson, M. B. Atkins, D. R. Byrd, A. C. Buzaid, A. J. Cochran *et al.*, "Final version of 2009 AJCC melanoma staging and classification," *J Clin Oncol* **27**, 6199–6206 (2009).
5. D. D. Witheiler and C. J. Cockerell, "Sensitivity of diagnosis of malignant melanoma: A clinicopathologic study with a critical assessment of biopsy techniques," *Exp Dermatol* **1**, 170–175 (1992).
6. L. Izikson, A. J. Sober, M. C. Mihm, Jr. and A. Zembowicz, "Prevalence of melanoma clinically resembling seborrheic keratosis: Analysis of 9204 cases," *Arch Dermatol* **138**, 1562–1566 (2002).
7. C. M. Grin, A. Kopf, B. Welkovich, R. Bart and M. Levenstein, "Accuracy in the clinical diagnosis of malignant melanoma," *Arc Dermatol* **126**, 763–766 (1990).

8. J. Mayer, "Systematic review of the diagnostic accuracy of dermatoscopy in detecting malignant melanoma," *Med J Aust* **167**, 206–210 (1997).
9. M. Binder, M. Schwarz, A. Winkler, A. Steiner, A. Kaider, K. Wolff and H. Pehamberger, "Epiluminescence microscopy: A useful tool for the diagnosis of pigmented skin lesions for formally trained dermatologists," *Arch Dermatol* **131**, 286–291 (1995).
10. M. Sadeghi, T. K. Lee, D. McLean, H. Lui and M. S. Atkins, "Global pattern analysis and classification of dermoscopic images using textons," In D. R. O. S. Haynor, editor, *Medical Imaging 2012: Image Processing* (2012).
11. M. Sadeghi, T. K. Lee, D. McLean, H. Lui and M. S. Atkins, "Detection and analysis of irregular streaks in dermoscopic images of skin lesions," *Ieee T Med Imaging* **32**, 849–861 (2013).
12. M. Sadeghi, M. Razmara, T. K. Lee and M. S. Atkins, "A novel method for detection of pigment network in dermoscopic images using graphs," *Comput Med Imaging Graph* **35**, 137–143 (2011).
13. H. Mirzaalian, T. K. Lee and G. Hamarneh, "Learning features for streak detection in dermoscopic color images using localized radial flux of principal intensity curvature", *IEEE Workshop on Mathematical Methods in Biomedical Image 2012*, Jan. 9–10, 2012, Breckenridge, Colorado, USA (2012).
14. P. Kharazmi and T. K. Lee, "Automatic segmentation of vascular patterns in dermoscopy images", *The 37th Canadian Medical and Biological Engineering Conference*, May 20–23, 2014, Vancouver, Canada (2014).
15. W. H. Clark, Jr., A. M. Ainsworth, E. A. Bernardino, C. H. Yang, C. M. Mihm, Jr. and R. J. Reed, "The developmental biology of primary human malignant melanomas," *Semin Oncol* **2**, 83–103 (1975).
16. H. Zhou, M. Chen, L. Zou, R. Gass, L. Ferris, L. Drogowski and J. M. Rehg, "Spatially constrained segmentation of dermoscopy images," *I S Biomed Imaging*, 800–803 (2008).
17. T. K. Lee, D. I. McLean and M. S. Atkins, "Irregularity index: A new border irregularity measure for cutaneous melanocytic lesions," *Medical Image Analysis* **7**, 47–64 (2003).
18. D. N. Vizireanu, "Generalizations of binary morphological shape decomposition," *J Electronic Imaging* **16**, 013002 (2007).
19. G. A. F. Seber, *Multivariate Observations*, John Wiley & Sons, Inc., Hoboken, New Jersey, (1984).
20. H. Spath, *The Cluster Dissection and Analysis Theory FORTRAN Programs Examples*, Prentice-Hall Inc., Upper Saddle River, New Jersey, (1985).
21. P. Wighton, T. K. Lee, H. Lui, D. I. McLean and M. S. Atkins, "Generalizing Common Tasks in Automated Skin Lesion Diagnosis," *IEEE Trans Information Techn Biomed* **15**, 622–629 (2011).
22. G. Argenziano, H. P. Soyer, S. Chimenti, R. Talamini, R. Corona, F. Sera, M. Binder, L. Cerroni *et al.*, "Dermoscopy of pigmented skin lesions: Results of a consensus meeting via the Internet," *J Am Acad Dermatol* **48**, 679–693 (2003).
23. M. E. Celebi, Y. A. Aslandogan, W. V. Stoecker, H. Iyatomi, H. Oka and X. H. Chen, "Unsupervised border detection in dermoscopy images," *Skin Res Techn* **13**, 454–462 (2007).

24. H. Iyatomi, H. Oka, M. Celebi, M. Hashimoto, M. Hagiwara, M. Tanaka and K. Ogawa, "An improved internet-based melanoma screening system with dermatologist-like tumor area extraction algorithm," *Comp Medical Imaging Graphics* **32**, 566–579 (2008).
25. M. Celebi, H. Kingravi, H. Iyatomi, Y. Aslandogan, W. Stoecker, R. Moss, J. Malters, J. Grichnik *et al.*, "Border detection in dermoscopy images using statistical region merging," *Skin Res Tech* **14**, 347–353 (2008).
26. M. Celebi, S. Hwang, H. Iyatomi and G. Schaefer, "Robust border detection in dermoscopy images using threshold fusion," *17th IEEE International Conference on Image Processing (ICIP)*, 2541–2544 (2010).
27. G. Argenziano, H. P. Soyer, V. D. Giorgio, D. Piccolo, P. Carli, M. Delfino, A. Ferrari, R. Hofmann-Wellenhof *et al.*, *Interactive Atlas of Dermoscopy*, Edra Medical Publishing and New Media, Milan, Italy (2000).
28. M. Hall, E. Frank, G. Holmes, B. Pfahringer, P. Reutemann and I. H. Witten, "The WEKA data mining software: an update," *SIGKDD Explorations* **11** (2009).